



Visualization of the strain-induced topological phase transition in a quasi-one-dimensional superconductor TaSe₃

Chun Lin¹, Masayuki Ochi², Ryo Noguchi¹, Kenta Kuroda¹, Masahito Sakoda^{1,3}, Atsushi Nomura⁴, Masakatsu Tsubota⁵, Peng Zhang¹, Cedric Bareille¹, Kifu Kurokawa¹, Yosuke Arai¹, Kaishu Kawaguchi¹, Hiroaki Tanaka¹, Koichiro Yaji^{1,6}, Ayumi Harasawa¹, Makoto Hashimoto^{1,7}, Donghui Lu¹, Shik Shin^{1,8}, Ryotaro Arita^{1,9,10}, Satoshi Tanda^{3,11} and Takeshi Kondo^{1,12}✉

Control of the phase transition from topological to normal insulators can allow for an on/off switching of spin current. While topological phase transitions have been realized by elemental substitution in semiconducting alloys, such an approach requires preparation of materials with various compositions. Thus it is quite far from a feasible device application, which demands a reversible operation. Here we use angle-resolved photoemission spectroscopy and spin- and angle-resolved photoemission spectroscopy to visualize the strain-driven band-structure evolution of the quasi-one-dimensional superconductor TaSe₃. We demonstrate that it undergoes reversible strain-induced topological phase transitions from a strong topological insulator phase with spin-polarized, quasi-one-dimensional topological surface states, to topologically trivial semimetal and band insulating phases. The quasi-one-dimensional superconductor TaSe₃ provides a suitable platform for engineering the topological spintronics, for example as an on/off switch for a spin current that is robust against impurity scattering.

Since the discovery of topological insulators (TIs)^{1–5}, many attempts have been made to control their fascinating properties. The most direct way is to use the phase transition from topological to normal insulator, which has been so far realized by elemental substitution in semiconducting alloys^{6–12}; the spin-orbit coupling and lattice constant are both varied simultaneously, leading to band inversion or eliminating it. To enable the reversible control of the phase transition, required for device application, using the strain effect, which can tune the lattice constant, would be a better and simpler approach. For this approach, we need to find a suitable material, which has the correct topological properties and can easily change its lattice constant by strain.

In the transition-metal trichalcogenides MX₃ (M = Nb, Ta; X = S, Se), physical properties vary and electronic orders evolve differently in accordance with the distinctive stacking sequences of the one-dimensional (1D) chain variants¹³. Among the series of MX₃, TaSe₃ is especially appealing in that superconductivity emerges at low temperatures (~2 K)¹⁴, in contrast with the other members, which typically undergo charge density wave transitions¹³. Due to its quasi-1D metallic character, it is proposed from the application point of view that TaSe₃ is suitable for the downscaled local interconnectors in electronic devices^{15,16}. More intriguingly, recent ab initio calculations predict that semimetallic TaSe₃ belongs to a three-dimensional (3D) strong TI phase¹⁷. This compound has been further suggested as a candidate for a topological superconductor¹⁷.

with advantages over other compounds^{18–26} in that the topological surface states (TSSs) are formed at the Fermi level (E_F); the superconductivity occurs in stoichiometric crystals without suffering from the doping-induced inhomogeneity; and the crystal structure is built from van der Waals stacking that is suitable for the application²⁷. Furthermore, this compound is in proximity to other topological phases, which thus potentially brings the attractive functionality of controlling the topological properties by the fine-tuning of a single physical parameter¹⁷.

The electronic structure of TaSe₃ was shown by angle-resolved photoemission spectroscopy (ARPES) more than a decade ago²⁸, as well as in a recent study with much better resolution²⁹. We use various types of ARPES techniques to observe the band structure of TaSe₃. In particular, spin-resolved ARPES (SARPES) with high momentum and energy resolutions is indispensable to identify the topological nature of this compound. Hence, we employ a laser-based SARPES that satisfies such requirements, and unambiguously reveal that TaSe₃ is indeed in a strong TI phase, as theory predicts. Moreover, two-step phase transitions are demonstrated by means of an in situ strain control of the band structure: by applying tensile strain to the samples, we observe a drastic evolution of the band structure, demonstrating the topological phase transition from a strong TI phase to a trivial semimetal phase. Upon further increase of the strain, the system eventually becomes a trivial band insulator, realizing the metal-insulator transition. The transition

¹Institute for Solid State Physics, University of Tokyo, Kashiwa, Japan. ²Department of Physics, Osaka University, Toyonaka, Japan. ³Department of Applied Physics, Hokkaido University, Kita-ku, Japan. ⁴Department of Physics, Tokyo University of Science, Tokyo, Japan. ⁵Department of Physics, Gakushuin University, Tokyo, Japan. ⁶Research Center for Advanced Measurement and Characterization, National Institute for Materials Science, Ibaraki, Japan.

⁷Stanford Synchrotron Radiation Lightsource, SLAC National Accelerator Laboratory, Menlo Park, CA, USA. ⁸Office of University Professor, University of Tokyo, Kashiwa, Japan. ⁹RIKEN Center for Emergent Matter Science, Wako, Japan. ¹⁰Department of Applied Physics, University of Tokyo, Tokyo, Japan.

¹¹Center of Education and Research for Topological Science and Technology, Hokkaido University, Kita-ku, Japan. ¹²Trans-scale Quantum Science Institute, University of Tokyo, Tokyo, Japan. ✉e-mail: kondo1215@issp.u-tokyo.ac.jp

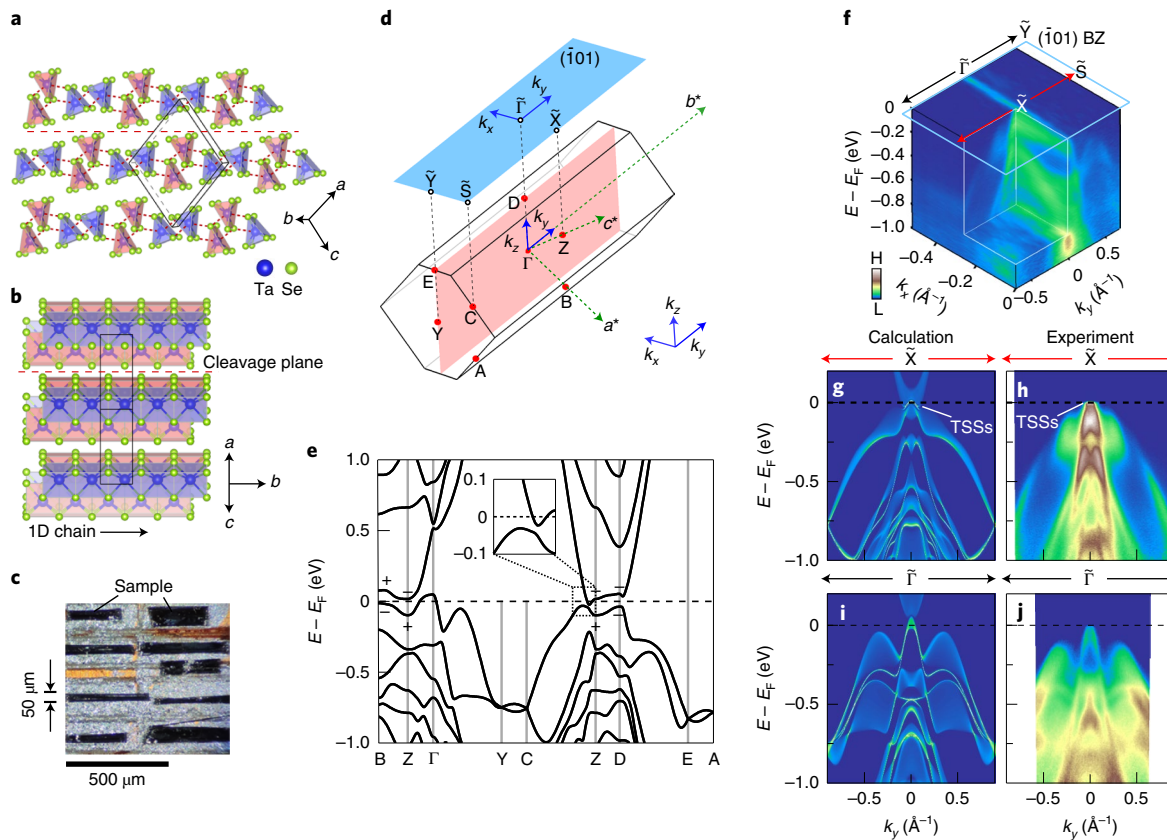


Fig. 1 | Crystal structure of TaSe_3 and its electronic structure revealed by ARPES. **a**, Crystal structure of TaSe_3 , stacked with two types of 1D chain with different bond lengths, as indicated by the reddish and bluish prisms. Adjacent 1D chains have an offset of $b/2$ along the chain direction, and the bonding between them is shown by the red dotted lines forming the $(\bar{1}01)$ layers, held in a stack by van der Waals forces. **b**, The side view of the crystal structure along the chain. The unit cell is indicated by the black lines, and the red dashed line marks the $(\bar{1}01)$ natural cleavage plane in both panels **a** and **b**. **c**, The image of the samples used for the ARPES measurements, indicating the typical crystal size with ~500 μm in length and 50–100 μm in width. **d**, A 3D bulk BZ and the projected $(\bar{1}01)$ surface BZ. The k_x and k_y are in plane, with the former perpendicular to the chain direction and the latter parallel to it; k_z is along the out-of-plane direction. a^* , b^* and c^* denote the reciprocal lattice vectors. **e**, Electronic structure of TaSe_3 with spin-orbit coupling. The parity eigenvalues at the B , Z and D points are indicated explicitly. **f**, A 3D plot of the band dispersion on the $(\bar{1}01)$ surface BZ (light blue box) probed by 50 eV photons. The colour bar represents the ARPES intensities from high (H) to low (L) in arbitrary units. **g,h**, Calculated TSSs and experimental band dispersion, respectively, across the X point in the momentum range indicated by the red arrows in **f**. The possible TSSs in **h** are also indicated. **i,j**, Calculated surface states and experimental band dispersion, respectively, across the $\tilde{\Gamma}$ point in the momentum range indicated by the black arrows in **f**. The photon energies used in **h** (50 eV) and **j** (30 eV) were selected so that the surface states were better resolved. See Supplementary Notes 2 and 3 and Supplementary Figs. 2 and 3 for more detailed discussions about the spectra obtained using different photon energies and polarizations.

from topologically non-trivial to trivial state is unique in TaSe_3 ; while the strain control of the topological state was previously attempted for Bi_2Se_3 (ref. ³⁰), the variation of the band structure by strain was rather small, exhibiting only a slight energy shift of the Dirac point. The uniaxial strain method was also effectively used to align the nematic superconducting domains in Sr-doped Bi_2Se_3 (ref. ³¹); such an effect, however, is not as drastic in the energy scale as that in the topological phase transition as realized in TaSe_3 . ZrTe_5 is another good system to use to control the topological phase via strain^{32,33}, but the transition proposed was between two non-trivial phases (the weak TI and strong TI phases), in contrast with the present results. Reversible control from the topological to non-topological phase in a single compound, TaSe_3 , without the necessity of elemental substitution as in alloys, opens up a new path towards applications in spintronics or optoelectronics. In particular, the controlling of the topological phase transition accompanied by superconductivity will bring entire new ideas for future applications.

The TaSe_3 crystal is built from the stacking of layers bonded together by weak van der Waals forces (Fig. 1a,b). As a result, we expect the $(\bar{1}01)$ plane to be at the surface after the sample is cleaved

(Fig. 1c), which has indeed been confirmed by our X-ray diffraction measurements (Supplementary Note 1 and Supplementary Fig. 1). The band structure calculated along high-symmetry momentum lines (Fig. 1d) is plotted in Fig. 1e; band inversion occurs around the Z point, opening an energy gap induced by the spin-orbit coupling effect (the inset of Fig. 1e). We have used synchrotron-ARPES with tunable photon energies to experimentally clarify the overall electronic structure of TaSe_3 . Figure 1f exhibits the overview of band dispersions observed on the $(\bar{1}01)$ surface Brillouin zone (BZ; Fig. 1d). In Fig. 1g–j, we compare the calculated surface-state spectra (left panels) and ARPES dispersions (right panels) across the X point (surface BZ edge, top panels) and $\tilde{\Gamma}$ point (surface BZ centre, bottom panels); a good agreement between the two is confirmed, regardless of the momentum cuts.

The surface and bulk states have distinct spectral properties and can be selectively enhanced by using proper photon energies and light polarizations (Supplementary Notes 2 and 3 and Supplementary Figs. 2 and 3). In Supplementary Fig. 2m,n, we plot the Fermi surface mappings and the constant-energy mappings at a high binding energy ($E_B=0.6$ eV), respectively, with different k_z values

along the out-of-plane direction (Fig. 1d) accessed by changing the photon energies. Unlike the mapping at $E_F = 0.6$ eV, the Fermi surface is found to be non-dispersive along k_z , suggesting that the low-energy, sharp features seen in Fig. 1h very likely come from surface states. The TSSs are expected, by calculations, to be confined in a limited momentum area around the \tilde{X} point and within a small bulk gap opened at E_F ; thus, ultra-high energy and momentum resolutions are required in ARPES experiments to visualize the predicted TSSs, and most importantly, the spin-resolved measurements at high resolution are indispensable to show that the surface states observed indeed have a topological origin.

The fine details of the low-energy electronic structure near \tilde{X} on the (101) surface BZ have been examined at high resolution by a 7 eV laser-ARPES equipped with a 3D spin-resolved detector. We focus on the momentum area in the red dashed square in Fig. 2a, surrounding the \tilde{X} point; calculations predict that the TSSs, characterized by sharp spectra near E_F , will emerge between the bulk conduction band (BCB) and bulk valence band (BVB) when approaching the \tilde{X} point, where these bands are inverted. In Fig. 2b–e, we compare the Fermi surfaces (top panels) and dispersions (bottom panels) across the \tilde{X} point, obtained by calculations (left panels) and ARPES (right panels); the ARPES data are also three-dimensionally displayed in Fig. 2f for better understanding. The low-energy spectra measured by laser-ARPES (Fig. 2c,e,f) clearly disentangle fine structures near the \tilde{X} point, which agree well with the calculated TSSs in the strong TI phase (Fig. 2b,d). To examine more details of the TSSs, we magnify the calculated and ARPES dispersions across \tilde{X} in Fig. 2i,j, respectively. The momentum distribution curves (MDCs) extracted at E_F (Fig. 2g,h) identify two pairs of TSSs (TSS_1 and TSS_2) and one pair of BCBs, indicating good consistency between the calculations and ARPES measurements. As detailed in Supplementary Fig. 4, the band dispersion of TSS_1 goes up in energy with increasing k_y along the in-plane direction (Fig. 1d) and merges into the BCB around $k_y = 0.1 \text{ \AA}^{-1}$, whereas that of TSS_2 goes down and merges into the BVB, just as expected for a strong TI phase (Fig. 2i). Spectra assigned to BCBs have relatively sharp peaks, unlike the continuum intensities for the surface band calculations (Fig. 2i), because of the following: ARPES at one photon energy, in principle, captures the band along a k_x - k_y sheet at a specific k_z , and thus can exhibit sharp peaks in the spectra not only for the surface band but also for the bulk band, while the latter could be suppressed by the k_z broadening in photoemission. This contrasts with the surface calculations, which project the bulk band spectra over the whole range of k_z .

To finalize our conclusion that TaSe_3 belongs to a strong TI phase, we demonstrate that the surface states we observed are spin-polarized, just as expected by the calculations. For this purpose, the experimental setting is now switched to the spin-resolved mode. Figure 2l plots the SARPES data, which map the spin k_x component (slightly off from the k_x direction in reality, due to the experimental geometry) measured for the energy-momentum region surrounded by the white dashed box in Fig. 2j; one can see how high the momentum resolution is in laser-SARPES compared with that in synchrotron-ARPES (Fig. 1h). To examine more details, we extract, in Fig. 2n–q, the spin-resolved energy distribution curves (EDCs) at the four specific k points indicated by arrows in Fig. 2j; the observed surface states are clearly spin-polarized (Supplementary Fig. 5 for the complete spin-polarization components). In Fig. 2r, the magnitude of spin-polarization is quantified for two outer k points with opposite signs ($+k_1$ and $-k_1$). The spin-polarization is reversed both with different energies and between $\pm k$. Intriguingly, we also found that these relationships on reversal are also swapped between different $|k|$ ($\pm k_1$ and $\pm k_2$), which yields a nodal point with spin degeneracy, possibly due to the band hybridization of TSSs. Note here that, while the spectral intensities in Fig. 2o are dominated by the down-spin (blue spectrum), mostly due to the matrix element effect, the spin degeneracy lifted by ~ 10 meV is clearly resolved, validating the spin-texture reversal. For clarity, the

experimentally obtained conclusion is summarized in Fig. 2m by showing the spin-integrated EDCs with red and blue colours assigned for up-spin and down-spin, respectively. All these features in the spin texture are reproduced well by calculations (Fig. 2k), showing that our experiments successfully captured the spin-momentum-locked TSSs, and hence established a strong TI phase in TaSe_3 . We note that TaSe_3 is not an insulator with a fully opened bulk gap in its strong TI phase, but a semimetal with a finite density of states at the Fermi level, which is a required condition to realize superconductivity, making this compound all the more fascinating for possible applications with topological superconductivity.

The quasi-1D structure is advantageous to modify the band structure effectively by uniaxial pressure. Hence, TaSe_3 built from chains is the ideal material to realize the strain-induced topological phase transition. Here we use the simplest technique of applying pressure to substances, which just mechanically bends a crystal on a substrate (Fig. 3a,b)³⁴, and reveal a systematic variation of the band structure under the tensile strain along the chain direction, which is controlled in situ. The samples were mounted on the sample platform of the strain device shown in Fig. 3a, by which tensile strain is applied via tightening four screws (Fig. 3b). We measured the amount of strain at the sample position using commercial strain gauges (Fig. 3c), and made a diagram relating the turning angle of the screws and the resulting strain (Fig. 3d), which was then used for the in situ strain control. The reliability of this diagram was evaluated by simulating the strain distribution in the device with finite element analysis (Fig. 3b); good agreement was confirmed between the simulation and the strain gauge measurements (Methods for more information about the strain device and the estimation of the strain).

Figure 3e–g presents the evolution of Fermi surface mappings by laser-ARPES with increasing tensile strain along the chain (0.2%, 1.1% and 2.4%, respectively), signifying two-step phase transitions. The high intensities seen at low strain (Fig. 3e) are significantly suppressed by applying higher strain (Fig. 3f), indicating that the TSSs disappear and thus the system has transitioned from a strong TI phase to a trivial semimetal phase; its semimetallic nature will be confirmed by comparisons with calculations in Fig. 4 and Supplementary Fig. 11. The vague intensities left for the bulk states (Fig. 3f) eventually vanish with further increase of the strain (Fig. 3g), revealing a transition of the system to a trivial band insulator phase, which opens a bulk gap at E_F .

More details of these two-step phase transitions are examined in Fig. 3h–s, which exhibits the evolution of band dispersions across \tilde{X} and $\tilde{\Gamma}$ (red and black arrows, respectively, in Fig. 3e–g), with gradually increasing tensile strain along the chain via in situ control. The highly intense signals due to TSSs are distinguished close to E_F at zero strain (Fig. 3h) and agree with the results in Fig. 2e; the differences in the spectral sharpness among these data mostly come from the different quality of the cleaved surfaces and different light polarizations used in the two different ARPES apparatuses used for the spin-texture and strain-control measurements (Supplementary Figs. 7 and 8 for TSSs obtained at different conditions). By applying tensile strain, the hole bands around \tilde{X} and $\tilde{\Gamma}$ both gradually shifted towards higher binding energies, demonstrating successful band-engineering by strain. The key features associated with the phase transitions are seen especially in close vicinity to E_F around the \tilde{X} point. The high intensities of TSSs seen at zero strain (Fig. 3h) were substantially suppressed at around 1% strain (Fig. 3j,k), which was then followed by a gap opening with larger strain (Fig. 3l,m). These behaviours are more directly demonstrated in Fig. 3t,u by extracting MDCs at E_F across \tilde{X} and EDCs at k_F (indicated by the white arrow in Fig. 3h) around \tilde{X} , respectively, which reveal the spectral evolution of TSSs (marked by red arrows in these panels). As the strain was increased in the strong TI phase, the TSSs became confined into a smaller momentum area (Fig. 3t), as a result of the reduced band inversion. Further increase of strain caused the

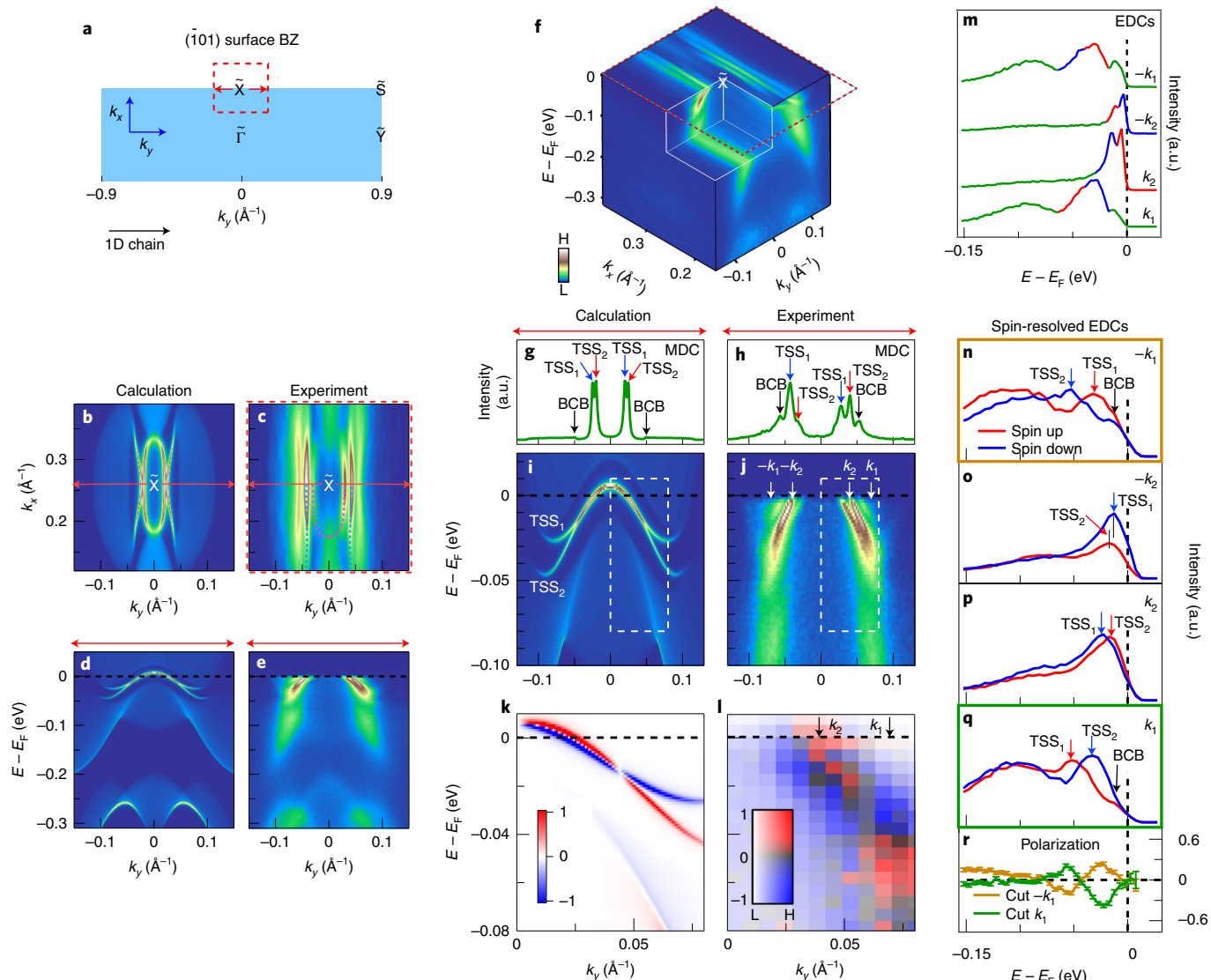


Fig. 2 | TSSs near the \tilde{X} point on the $(\bar{1}01)$ surface BZ revealed by laser-SARPES with 7 eV photons. **a**, Schematic of the $(\bar{1}01)$ surface BZ. **b,c**, Calculated and experimental surface-state Fermi surfaces within the momentum range around the \tilde{X} point specified by the red dashed rectangle in **a**. The dashed curves in **c** depict the contour of the TSSs. **d,e**, Calculated and experimental surface-state dispersions at the \tilde{X} point with momentum positions indicated by the red arrows in **b** and **c**. **f**, The 3D plot of the experimental surface-state dispersion around the \tilde{X} point. The spectra in **c** and **f** are symmetrized with respect to the zone edge. The colour bar represents the ARPES intensities from high (H) to low (L) in arbitrary units. **g,h**, Calculated and experimental MDCs at E_F along the red arrows in **b** and **c**, respectively, indicating the correspondences of the two branches of the TSSs (TSS_1 , TSS_2) and BCBs. **i,j**, Magnified calculated and experimental TSSs for **d** and **e**, respectively. **k,l**, Calculated spin texture and experimental spin-polarization map, respectively, with energy-momentum range specified by the white dashed rectangles in **i** and **j**. The colour bar in **k** represents the spin-polarization magnitude. The spin-polarization map in **l** is coded by a two-dimensional colour scale with horizontal and vertical axes indicating the spectral weight and the polarization, respectively. The spin-polarization vector is nearly in plane and perpendicular to the chain direction; the complete spin-polarization components are in Supplementary Fig. 5. **m-q**, Spin-integrated (**m**) and spin-resolved (**n-q**) EDCs of the TSSs at the four momentum cuts indicated in **j**. **r**, Representative spin-polarization magnitude for outer two cuts, $-k_1$ and k_1 , whose spin-resolved EDCs are shown in **n** and **q** with borders highlighted by the corresponding colour.

spectral peaks of the TSSs to disappear by eliminating the band inversion, and consequently the system transitioned to a trivial semimetal phase. Eventually, the strain got large enough to reopen the band gap, which totally eliminated the spectral intensity around E_P and thus the system transitioned to a trivial insulator phase. A previous study has shown an anomalous strain effect on the resistivity, which increased by several orders of magnitude when the applied strain along the chain reached $\sim 0.6\%$ (ref. 35), in agreement with our observation of the band structure and the depletion of the spectral intensity at E_P , shown in Fig. 3v.

To fully understand the mechanism of the phase transitions we observed, ab initio calculations were performed for $TaSe_3$ under strain along the chain direction. The evolution of the bulk electronic structure in the calculations (Fig. 4b-d) nicely illustrates the mechanism of the phase transition induced by reducing and eliminating the band inversion with increasing tensile strain, which are manifested as the closing and reopening of a gap at the Z point. The calculated surface spectra of the Fermi surface (Fig. 4f-h) and energy dispersions (Fig. 4k-p) across \tilde{X} and $\tilde{\Gamma}$ both reproduce our observations well, of two-step phase transitions from a strong

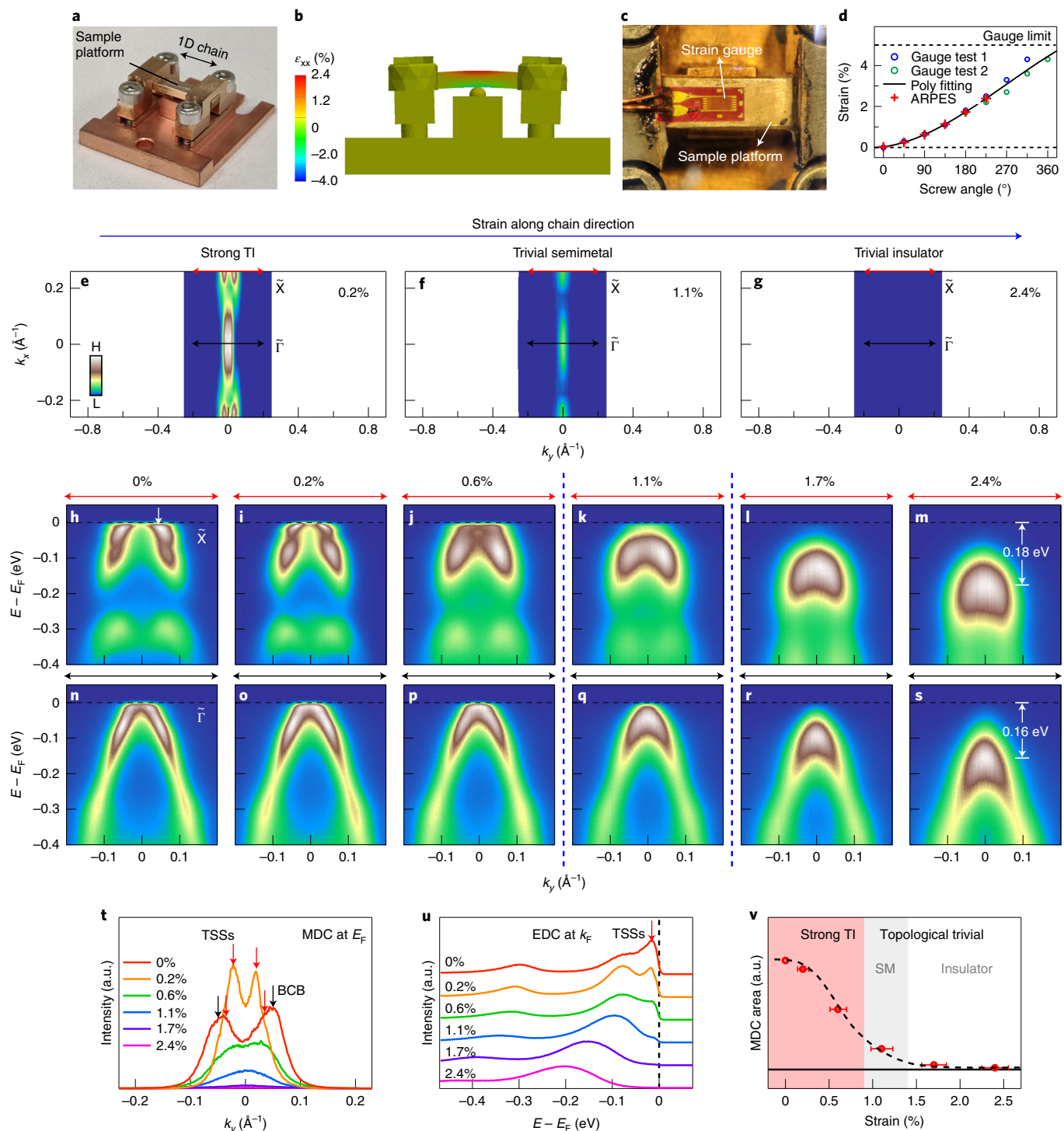


Fig. 3 | Observed topological and metal-insulator phase transitions driven by the in-situ-controlled tensile strain along the chain. **a**, The strain device. The samples were mounted on the sample platform with the 1D chain along the length. **b**, Side view of the device with colours encoding the simulated longitudinal strain distribution (ϵ_{xx}). **c**, The commercial strain gauge attached to a sample platform. **d**, Strain magnitude versus screw angles for two representative tests measured by the strain gauges. The red markers indicate the strain magnitude in the ARPES measurements obtained by interpolating the fitting curve at the corresponding screw angles controlled in situ. Poly, polynomial. **e–g**, Measured Fermi surfaces in the strong TI, trivial semimetal and trivial insulator phases with a strain of 0.2%, 1.1% and 2.4%, respectively. The spectra are symmetrized with respect to $k_x = 0$. The colour bar in **e** represents the ARPES intensities from high (H) to low (L) in arbitrary units. **h–m**, Dispersions at the \tilde{X} point with increasing strain, indicated on the top of each panel. **n–s**, Corresponding dispersions at the $\tilde{\Gamma}$ point. The energy positions of the intensity maxima are indicated in **m** and **s**. **t,u**, MDCs at E_F (**t**) and EDCs at k_F (**u**) near the \tilde{X} point with different strain values. The k_F position of the TSSs is indicated by the white arrow in **h**. **v**, Evolution of the spectral intensity at E_F (MDC area in **t**) with different strain values. The dashed line is a guide for the eyes. SM, semimetal. See the Methods for more details, including the error bars.

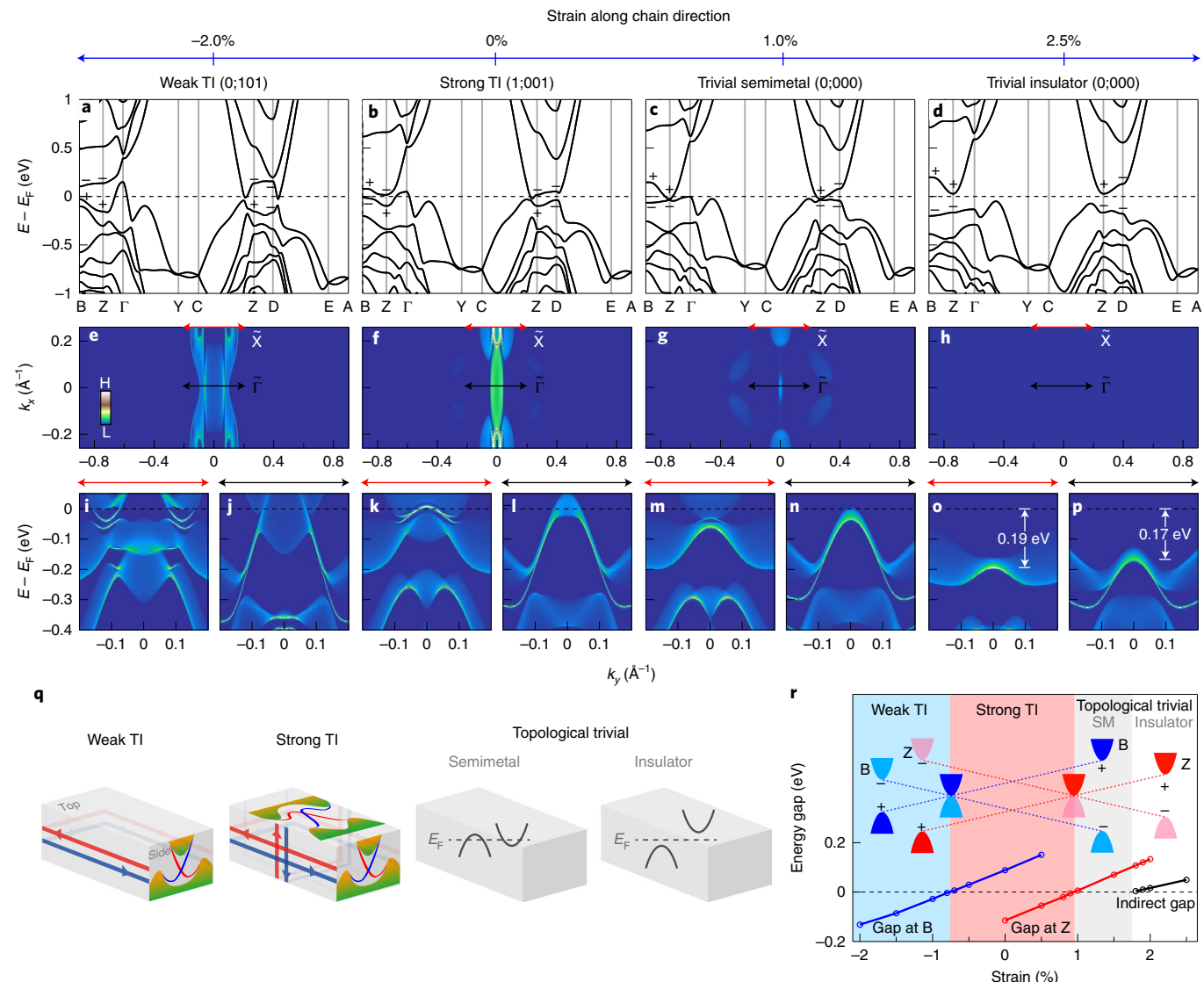


Fig. 4 | Calculated topological phase transition and metal–insulator transition driven by the strain along chain direction. **a–d**, Electronic structures in the weak TI, strong TI, trivial semimetal and trivial insulator phases under the strain values indicated on the top. The Z_2 invariants for each phase are indicated at the top of each panel. The parity eigenvalues at the B, Z and D points where band inversions occur are indicated explicitly. **e–h**, Corresponding Fermi surfaces for **a–d**, respectively, on the $(\bar{1}01)$ surface. The colour bar in **e** represents the spectral intensities from high (H) to low (L) in arbitrary units. **i–p**, Corresponding band dispersions across the \bar{X} (**i,k,m,o**) and \bar{T} (**j,l,n,p**) points with momentum ranges indicated by the red and black arrows in **e–h**, respectively. The energy positions of the intensity maxima are indicated in **o** and **p**, which nicely match the energy scales in Fig. 3m,s. **q**, Schematics of the surface spin current, TSSs, or bulk band structure in different phases. The dispersions of TSSs are shown on the crystal surfaces (on all surfaces in the strong TI phase and only on the side surface in the weak TI phase). Red and blue represent a spin-up current (state) and a spin-down current (state), respectively. **r**, Calculated strain phase diagram of TaSe_3 . The direct gaps at the Z and B points, as well as the indirect gap (defined by the energy difference between the conduction band bottom and valence band top) are plotted as a function of strain along the chain. The zero-energy crossing points of these energy scales define the quantum critical points of approximately -0.75% , 0.95% and 1.75% for the three phase transitions, from weak TI to strong TI, to trivial semimetal, to trivial band insulator phases. The schematics indicate the evolutions of the bulk band energies and the parity inversions at the Z and B points across the topological quantum critical points.

TI phase to a trivial semimetal phase, and then to a trivial band insulator phase, with increasing tensile strain up to 2.5% , which is comparable to the maximum strain value in our experiments. The spectral agreement between experimental observations (Fig. 3f,k,q in the semimetal phase and Fig. 3g,m,s in the insulator phase) and calculations (Fig. 4g,m,n and Fig. 4h,o,p, respectively) is excellent (Supplementary Figs. 11 and 12 for direct comparisons).

We also calculated the effect of compressive strain on TaSe_3 (Fig. 4a,e,i,j); it not only enlarges the band inversion at the Z point, but also inverts another band at the B point (Fig. 4a), triggering an

additional topological phase transition from a strong TI phase to a weak TI phase, where the TSSs emerge only at the side surface (Fig. 4q). Applying compressive strain to quasi-1D crystals is experimentally very challenging since a compression in the chain direction easily bends or wrinkles the crystals, which releases the compressive force before reaching the amount one intends to apply. Even so, we have applied compressive strain to some extent and successfully observed the enhancement of band inversion, which indicates that the system was driven towards the weak TI phase by the compressive strain, as calculations predict (Supplementary Figs. 13

and 14); nevertheless, the decisive evidence for the weak TI phase is lacking, so we leave it for a future work.

In Fig. 4r, we summarize the evolution of the direct energy gaps at B and Z, which determines the bulk topology, and also the indirect gap of the system, which reveals the metallic nature of TaSe₃, with strain applied along the chain δ_b . The topological quantum critical points have been obtained at $\delta_b \approx -0.75\%$ and 0.95% ; the band inversion occurs at both B and Z for $\delta_b < -0.75\%$, and only at Z for $-0.75\% < \delta_b < 0.95\%$, and eventually it is ruled out for $\delta_b > 0.95\%$. At these three values, a weak TI, a strong TI, and a trivial semimetal phase appear, respectively. Moreover, we also found another type of critical point at $\delta_b \approx 1.75\%$, across which the metal–insulator transition occurs. The correspondence between the δ_b values applied and the electronic phases obtained in calculations matches surprisingly well with our experimental results (Fig. 3v).

The strain-induced topological phase transition can be generally interpreted as follows. The tensile strain increases the distance among the atoms building the crystal, which suppresses the hopping integral of electrons and thus shrinks the electronic bands. As a result, the overlapping of the conduction and valence bands is diminished, and eventually, the band inversion is removed with enough strain, causing the transition from the non-trivial topological phase to the trivial phase. The calculations in Fig. 4b–d clearly show that the valence bands are narrowed as tensile strain increases, removing the band inversion and eventually opening the full band gap. The opposite occurs with compressive strain (Fig. 4a): the electronic bands expand due to the larger hopping integral of electrons, which enhances the overlapping of the conduction and valence bands. Consequently, another band inversion occurs, causing the transition from the strong TI phase to the weak TI phase.

The quasi-1D topological state of a superconductor TaSe₃ that we have revealed could have several scientific and technological implications. In particular, TaSe₃ has an excellent functionality in that the band topology is easily controlled by mechanical strain, leading to the reversible on/off switching of highly directional, dense spin currents that are protected from impurity scattering (Supplementary Fig. 10 for the reversibility). To date, the topological phase transition from a strong TI phase to a trivial insulator phase has been observed directly by ARPES for alloys, where the bulk topology is controlled by elemental substitution, which varies both the lattice constant and the spin–orbit coupling strength. Here we have demonstrated a method that tunes only the lattice constant by strain, and that is much simpler, reversible, and thus promising for future applications. Hence, our experimental observations of the topological phase transition between a strong TI state and a trivial state, realized in a superconductor, will prompt further basic and technological research for engineering topological spintronics or optoelectronics that exploit the topological phase transition and the interplay of topological state with superconductivity, likely leading to the topological superconducting state. While further work is required, the expectation of the ability to control the Majorana fermions will encourage follow-up research on new strategies for realizing quantum computation.

Online content

Any methods, additional references, Nature Research reporting summaries, source data, extended data, supplementary information, acknowledgements, peer review information; details of author contributions and competing interests; and statements of data and code availability are available at <https://doi.org/10.1038/s41563-021-01004-4>.

Received: 14 September 2020; Accepted: 1 April 2021;
Published online: 20 May 2021

References

- Fu, L., Kane, C. L. & Mele, E. J. Topological insulators in three dimensions. *Phys. Rev. Lett.* **98**, 106803 (2007).
- Fu, L. & Kane, C. L. Topological insulators with inversion symmetry. *Phys. Rev. B* **76**, 045302 (2007).
- Hasan, M. Z. & Kane, C. L. Colloquium: topological insulators. *Rev. Mod. Phys.* **82**, 3045 (2010).
- Qi, X.-L. & Zhang, S.-C. Topological insulators and superconductors. *Rev. Mod. Phys.* **83**, 1057 (2011).
- Ando, Y. Topological insulator materials. *J. Phys. Soc. Jpn.* **82**, 102001 (2013).
- Xu, S.-Y. et al. Topological phase transition and texture inversion in a tunable topological insulator. *Science* **332**, 560–564 (2011).
- Sato, T. et al. Unexpected mass acquisition of Dirac fermions at the quantum phase transition of a topological insulator. *Nat. Phys.* **7**, 840–844 (2011).
- Xu, S.-Y. et al. Observation of a topological crystalline insulator phase and topological phase transition in Pb_{1-x}Sn_xTe. *Nat. Commun.* **3**, 1192 (2012).
- Brahlek, M. et al. Topological-metal-to-band-insulator transition in (Bi_{1-x}In_x)₂Se₃ thin films. *Phys. Rev. Lett.* **109**, 186403 (2012).
- Zhang, J. et al. Topology-driven magnetic quantum phase transition in topological insulators. *Science* **339**, 1582–1586 (2013).
- Wu, L. et al. A sudden collapse in the transport lifetime across the topological phase transition in (Bi_{1-x}In_x)₂Se₃. *Nat. Phys.* **9**, 410–414 (2013).
- Xu, S.-Y. et al. Unconventional transformation of spin Dirac phase across a topological quantum phase transition. *Nat. Commun.* **6**, 6870 (2015).
- Monceau, P. Electronic crystals: an experimental overview. *Adv. Phys.* **61**, 325–581 (2012).
- Samboni, T. et al. Superconductivity in one-dimensional TaSe₃. *J. Phys. Soc. Jpn.* **42**, 1421–1422 (1977).
- Stolyarov, M. A. et al. Breakdown current density in h-BN-capped quasi-1D TaSe₃ metallic nanowires: prospects of interconnect applications. *Nanoscale* **8**, 15774–15782 (2016).
- Liu, G. et al. Low-frequency electronic noise in quasi-1D TaSe₃ van der Waals nanowires. *Nano Lett.* **17**, 377–383 (2017).
- Nie, S. et al. Topological phases in the TaSe₃ compound. *Phys. Rev. B* **98**, 125143 (2018).
- Fu, L. & Berg, E. Odd-parity topological superconductors: theory and application to Cu_xBi₂Se₃. *Phys. Rev. Lett.* **105**, 097001 (2010).
- Sasaki, S. et al. Topological superconductivity in Cu_xBi₂Se₃. *Phys. Rev. Lett.* **107**, 217001 (2011).
- Wang, M.-X. et al. The coexistence of superconductivity and topological order in the Bi₂Se₃ thin films. *Science* **336**, 52–55 (2012).
- Mourik, V. et al. Signatures of Majorana fermions in hybrid superconductor–semiconductor nanowire devices. *Science* **336**, 1003–1007 (2012).
- Sakano, M. et al. Topologically protected surface states in a centrosymmetric superconductor β -PdB₂. *Nat. Commun.* **6**, 8595 (2015).
- Guan, S.-Y. et al. Superconducting topological surface states in the noncentrosymmetric bulk superconductor PbTaSe₃. *Sci. Adv.* **2**, e1600894 (2016).
- Zhang, P. et al. Observation of topological superconductivity on the surface of an iron-based superconductor. *Science* **360**, 182–186 (2018).
- Clark, O. J. et al. Fermiology and superconductivity of topological surface states in PdTe₂. *Phys. Rev. Lett.* **120**, 156401 (2018).
- Liu, W. et al. A new Majorana platform in an Fe-As bilayer superconductor. *Nat. Commun.* **11**, 5688 (2020).
- Yuan, Y. et al. Evidence of anisotropic Majorana bound states in 2M-WS₂. *Nat. Phys.* **15**, 1046–1051 (2019).
- Peruchi, A. et al. Spectroscopic and dc-transport investigations of the electronic properties of TaSe₃. *Eur. Phys. J. B* **39**, 433–440 (2004).
- Chen, C. et al. Observation of topological electronic structure in quasi-1D superconductor TaSe₃. *Matter* **3**, 2055–2065 (2020).
- Flöttotto, D. et al. In situ strain tuning of the Dirac surface states in Bi₂Se₃ films. *Nano Lett.* **18**, 5628–5632 (2018).
- Kostylev, I., Yonezawa, S., Wang, Z., Ando, Y. & Maeno, Y. Uniaxial-strain control of nematic superconductivity in Sr_xBi₂Se₃. *Nat. Commun.* **11**, 4152 (2020).
- Mutch, J. et al. Evidence for a strain-tuned topological phase transition in ZrTe₅. *Sci. Adv.* **5**, eaav9771 (2019).
- Zhang, P. et al. Observation and control of the weak topological insulator state in ZrTe₅. *Nat. Commun.* **12**, 406 (2021).
- Ricciò, S. et al. In situ strain tuning of the metal-insulator-transition of Ca₃RuO₄ in angle-resolved photoemission experiments. *Nat. Commun.* **9**, 4535 (2018).
- Tritt, T. M., Stillwell, E. P. & Skove, M. J. Effect of uniaxial stress on the transport properties of TaSe₃. *Phys. Rev. B* **34**, 6799 (1986).

Publisher's note Springer Nature remains neutral with regard to jurisdictional claims in published maps and institutional affiliations.

© The Author(s), under exclusive licence to Springer Nature Limited 2021,
corrected publication 2021

Methods

Samples. High-quality monoclinic whisker crystals of TaSe₃ were synthesized by the vapour phase transport method, with lattice constants $a = 10.405 \text{ \AA}$, $b = 3.499 \text{ \AA}$, $c = 9.826 \text{ \AA}$ and $\beta = 106.26^\circ$ (ref. ³⁶). Typical samples used for the ARPES and SARPES measurements are shown in Fig. 1c with an in-plane dimension of $\sim 500 \times 50$ to $\sim 500 \times 100 \mu\text{m}^2$. The samples used in the strain-dependent measurements were intentionally selected to be as small and thin as possible (generally $500 \times 50 \times 2 \mu\text{m}^3$), to diminish any strain relaxation effects. More details can be found in Supplementary Note 1.

ARPES. Synchrotron-based ARPES measurements were performed at beamline 5-2 of the Stanford Synchrotron Radiation Lightsource with tunable photon energies from 25 eV to 100 eV. The spot size was $\sim 0.04 \text{ mm}^2$ (horizontal) $\times 0.01 \text{ mm}^2$ (vertical), and the equipped ScientaOmicron DA30L analyser enabled full access of the momentum space without sample rotation; both of these facts facilitated the measurements, as the typical sample width was ~ 50 – $100 \mu\text{m}$. The light polarization used was linear vertical (along the analyser slit), with the overall energy resolution from 10–20 meV and angular resolution better than 0.2° ; Supplementary Notes 2 and 3 and Supplementary Figs. 2 and 3 have more detailed discussions about the photon energy and light polarization dependences of the spectra. The samples were cleaved using an exfoliation method and measured *in situ* at a temperature of $\sim 10 \text{ K}$ and a pressure lower than $3 \times 10^{-11} \text{ torr}$.

The laser-based SARPES³⁷ measurements were performed at the Institute for Solid State Physics, University of Tokyo, which is equipped with 6.994 eV photons and a ScientaOmicron DA30L analyser. The laser was p-polarized with a spot size of $\sim 0.05 \text{ mm}^2$. Supplementary Notes 5 and 6 and Supplementary Figs. 5 and 6 have more information about the laser polarizations and apparatus geometry. The energy (angular) resolution was set at better than 2 meV (0.2°) and 15 meV (0.7°) for ARPES and SARPES, respectively. The samples were cleaved using a similar method at room temperature with a pressure less than $5 \times 10^{-9} \text{ torr}$, and measured at $\sim 10 \text{ K}$ with a pressure less than $7 \times 10^{-11} \text{ torr}$. The spin-polarization map in Fig. 2l utilizes a two-dimensional colour coding with horizontal and vertical axes indicating the spectral weight and the polarization, respectively^{38,39}.

The strain-dependent laser-ARPES measurements were performed in similar conditions to SARPES but with a ScientaOmicron R4000 analyser. The angular resolution was $\sim 0.3^\circ$, and the laser polarization was linear horizontal (along the analyser slit). More information about laser polarizations and apparatus geometry is shown in Supplementary Fig. 2. The samples were mounted on the strain device using silver epoxy (Muromac H-220), cleaved *in situ* at room temperature with a pressure less than $1 \times 10^{-10} \text{ torr}$ and measured at a temperature $< 10 \text{ K}$ with a pressure of $\sim 1 \times 10^{-11} \text{ torr}$. The *in-situ* strain controls were realized by rotating the screws 45° step by step at a temperature of $< 30 \text{ K}$ with a pressure less than $5 \times 10^{-10} \text{ torr}$. The typical time for one 45° rotation was $\sim 2 \text{ min}$, and we confirmed that there was no surface ageing by performing strain control cycles and measuring *at freshly cleaved samples with strain applied ex situ* (Supplementary Fig. 10). We also show the *in-situ* strain-control reversibility test in Supplementary Fig. 10; the results indicate that the strain effects are completely reversible. After each measurement, we monitored the device status, and estimated and calibrated the *in-situ*-controlled strain magnitude to the strain measured by the strain gauges, as described below.

Strain evaluation. The strain device³⁴ was specially designed for the low-energy laser-ARPES apparatus. The key components of the device include two BeCu bridges, one BeCu sample platform ($10 \times 2 \times 1 \text{ mm}^3$) and one Si₃N₄ ball (1 mm diameter) below the platform. When the screws are tightened, the sample platform is bent by the bridges, providing uniaxial strain to the mounted samples, as demonstrated in Fig. 3b. As the laser spot size is small, we found no evidence of spectral broadening due to possible domains introduced by bending. Good thermal (electric) conductivity has been confirmed by comparing the spectra with those obtained from samples mounted on normal sample holders.

The strain magnitude as a function of screw angle (Fig. 3d) was measured by the commercial strain gauges (Fig. 3c, Kyowa KFGS-1N-120-C1-11) at room temperature. For both the strain gauge measurements and the strain-dependent ARPES measurements, we always carefully adjusted the screws and platforms to ensure the initial conditions of the devices were identical within error bars. Before the measurements, the heights of the four screws and the bridges were equally adjusted to ensure a flat platform. Meanwhile, the displacements between the centre of the sample platform and its contact positions with the bridges were carefully monitored, so that a zero net strain was ensured before attaching the strain gauges or mounting samples. We have conducted several strain gauge measurements on different devices and obtained similar results (two of them are shown in Fig. 3d). By fitting the data with a polynomial function (the black curve in Fig. 3d), we can estimate the strain magnitude, *in situ* controlled, during the ARPES measurements by interpolating at the corresponding screw angles. We also measured the displacement as a function of the strain, as shown in Supplementary Fig. 9d. Comparing to the large strain in our experiments ($\sim 2.4\%$), we ignore the thermal contraction, which is typically approximately -0.2% according to our thermal-strain simulations. The error bars for the strain magnitude controlled in the ARPES measurements were estimated in accordance with the uncertainty of the screw angles and are shown in Fig. 3d,v (smaller than the marker size in Fig. 3d).

The strain simulations based on finite element analysis were performed when the platform displacement reached 0.124 mm (Supplementary Fig. 9d,g), using the Autodesk Inventor 2020. For the BeCu components, a Young's modulus of 120 GPa and a Poisson's ratio of 0.3 were implemented. Figure 3b and Supplementary Fig. 9e show the simulated axial strain (ϵ_{xx}) distribution on the sample platform. The ϵ_{xx} value reached the maximum of $\sim 2.4\%$ at the platform centre, nicely consistent with our experimental results from the strain gauges at the same displacement (Supplementary Fig. 9d). The transverse strain (ϵ_{yy}) distribution is shown in Supplementary Fig. 9f, which reached the minimum of approximately -0.2% at the platform centre. Supplementary Fig. 9h summarizes the overall strain distribution by plotting the ϵ_{xx} and ϵ_{yy} values as a function of coordinates along x ($y = 0$) and along y ($x = 0$), respectively. We note that the samples used for strain-dependent ARPES measurements were very small (generally $500 \times 50 \times 2 \mu\text{m}^3$) and mounted at the centre of the platform. Therefore, the tiny transverse strain perpendicular to the platform is negligible. Moreover, as the samples used were also very thin, our simulations show that the strain on the sample surface was almost the same as that on the platform centre (Supplementary Fig. 9i,j). Supplementary Notes 9 and 10 have more detailed descriptions about the strain devices, strain evaluation and *in-situ* strain controls.

Density functional theory calculations. First, we performed the structural optimization using the Perdew–Burke–Ernzerhof exchange–correlation functional revised for solids⁴⁰ and the projector augmented wave method⁴¹ as implemented in the Vienna Ab initio Simulation Package^{42–45}. The spin-orbit coupling was included in all the calculations presented in this paper. Here, we optimized atomic coordinates while the lattice parameters were fixed as our experimental values. We also optimized atomic coordinates in the strain calculations, where the lattice parameters except for b (the length along the strain direction) were fixed as unstrained values for simplicity. Next, we performed first-principles band-structure calculations using the modified Becke–Johnson potential⁴⁶ as implemented in the WIEN2K code⁴⁷. The muffin-tin radii r for Ta and Se were set to 2.5 and 2.39 a.u., respectively, for the unstrained calculation, while they were slightly changed for the strained calculations. The maximum modulus for the reciprocal lattice vectors K_{\max} was chosen so that $r_s K_{\max} = 8$. We took a $4 \times 12 \times 4 k$ mesh for a self-consistent-field calculation, while a following non-self-consistent-field calculation to determine the Fermi energy was performed using a finer k mesh, up to 25,000 points. From the calculated band structures, we extracted the Wannier functions of the Ta s and d orbitals and the Se s and p orbitals using the WIEN2WANNIER and WANNIER90 codes^{48–51}. We did not perform the maximal localization procedure for the Wannier functions to prevent orbital mixing among the different spin components. The semi-infinite-slab tight-binding models constructed from these Wannier functions were used for calculating the surface spectra in a way described in the literature⁴². The Fermi energy in all the calculated data is shifted by -10 meV so as to reproduce the experimental spectra.

The tensile strain along the chain direction leads to finite compressive strain perpendicular to it, due to the Poisson effect. However, we did not take the perpendicular compressive strain into account in the density functional theory calculations of Fig. 4 since the effect is negligible and not crucial for our conclusions. To confirm this, we have performed a simulation considering Poisson's ratio and estimated the perpendicular strain to be only -0.2% when the tensile strain along the chain direction was set to 2.4% (Supplementary Fig. 9h), which is the maximum value we applied for the samples in our experiments. Subsequently, we calculated the bulk band structure under the 2.4% tensile strain along the chain direction with and without the effect of the perpendicular compressive strain of -0.2% ; no considerable difference was obtained between the two (Supplementary Fig. 15), leading us to conclude that the effect of the perpendicular compressive stain can be ignored in our study.

Data availability

The data that support the findings of this study are available from the corresponding author upon request.

References

36. Nomura, A. et al. Emergence of a resistance anomaly by Cu-doping in TaSe₃. *EPL* **119**, 17005 (2017).
37. Yaji, K. et al. High-resolution three-dimensional spin- and angle-resolved photoelectron spectrometer using vacuum ultraviolet laser light. *Rev. Sci. Instrum.* **87**, 053111 (2016).
38. Tusche, C., Krasyluk, A. & Kirschner, J. Spin resolved bandstructure imaging with a high resolution momentum microscope. *Ultramicroscopy* **159**, 520–529 (2015).
39. Noguchi, R. et al. Direct mapping of spin and orbital entangled wave functions under interband spin-orbit coupling of giant Rashba spin-split surface states. *Phys. Rev. B* **95**, 041111 (2017).
40. Perdew, J. P. et al. Restoring the density-gradient expansion for exchange in solids and surfaces. *Phys. Rev. Lett.* **100**, 136406 (2008).
41. Kresse, G. & Joubert, D. From ultrasoft pseudopotentials to the projector augmented-wave method. *Phys. Rev. B* **59**, 1758 (1999).

42. Kresse, G. & Hafner, J. Ab initio molecular dynamics for liquid metals. *Phys. Rev. B* **47**, 558 (1993).
43. Kresse, G. & Hafner, J. Ab initio molecular-dynamics simulation of the liquid-metal-amorphous-semiconductor transition in germanium. *Phys. Rev. B* **49**, 14251 (1994).
44. Kresse, G. & Furthmüller, J. Efficiency of ab-initio total energy calculations for metals and semiconductors using a plane-wave basis set. *Comput. Mater. Sci.* **6**, 15–50 (1996).
45. Kresse, G. & Furthmüller, J. Efficient iterative schemes for ab initio total-energy calculations using a plane-wave basis set. *Phys. Rev. B* **54**, 11169 (1996).
46. Tran, F. & Blaha, P. Accurate band gaps of semiconductors and insulators with a semilocal exchange-correlation potential. *Phys. Rev. Lett.* **102**, 226401 (2009).
47. Blaha, P. et al. *WIEN2k: An Augmented Plane Wave Plus Local Orbitals Program for Calculating Crystal Properties* (Technische Universität Wien, 2018).
48. Marzari, N. & Vanderbilt, D. Maximally localized generalized Wannier functions for composite energy bands. *Phys. Rev. B* **56**, 12847 (1997).
49. Souza, I., Marzari, N. & Vanderbilt, D. Maximally localized Wannier functions for entangled energy bands. *Phys. Rev. B* **65**, 035109 (2001).
50. Kuneš, J. et al. Wien2wannier: from linearized augmented plane waves to maximally localized Wannier functions. *Comput. Phys. Commun.* **181**, 1888–1895 (2010).
51. Pizzi, G. et al. Wannier90 as a community code: new features and applications. *J. Phys. Condens. Matter* **32**, 165902 (2020).
52. Lopez Sancho, M. P., Lopez Sancho, J. M., Sancho, J. M. L. & Rubio, J. Highly convergent schemes for the calculation of bulk and surface green functions. *J. Phys. F Met. Phys.* **15**, 851 (1985).

Acknowledgements

We thank D. Hirai and Y. Mizukami for fruitful comments on the strain measurements, and also thank S. Sakuragi and T. Yajima for the X-ray diffraction measurements. Use of

the Stanford Synchrotron Radiation Lightsource, SLAC National Accelerator Laboratory, is supported by the US Department of Energy, Office of Science, Office of Basic Energy Sciences under contract no. DE-AC02-76SF00515. This work was supported by the JSPS KAKENHI (grant numbers JP18H01165, JP18K03484, JP19H02683, JP19F19030 and JP19H00651), MEXT Q-LEAP (grant number JPMXS0118068681) and by MEXT under the ‘Program for Promoting Researches on the Supercomputer Fugaku’ (Basic Science for Emergence and Functionality in Quantum Matter Innovative Strongly Correlated Electron Science by Integration of ‘Fugaku’ and Frontier Experiments; project ID hp200132).

Author contributions

T.K. and S.T. planned the experimental project. C.L. conducted the ARPES experiments, analysed the data and performed the strain simulations. C.L. and T.K. designed the strain devices. C.L., K. Kuroda, Y.A. and T.K. conducted the strain gauge measurements. R.N., K. Kuroda, P.Z., C.B., K. Kurokawa, Y.A., K. Kawaguchi, H.T., K.Y., A.H., M.H., D.L., S.S. and T.K. supported the ARPES experiment. M.S., A.N., M.T. and S.T. prepared the single crystals. M.O. and R.A. calculated and analysed the theoretical band structure. C.L., M.O. and T.K. wrote the paper. All authors discussed the results and commented on the manuscript.

Competing interests

The authors declare no competing interests.

Additional information

Supplementary information The online version contains supplementary material available at <https://doi.org/10.1038/s41563-021-01004-4>.

Correspondence and requests for materials should be addressed to T.K.

Peer review information *Nature Materials* thanks Phil King, Hsin Lin and the other, anonymous, reviewer(s) for their contribution to the peer review of this work.

Reprints and permissions information is available at www.nature.com/reprints.